

Homing through Reinforcement Learning

Riya Singh^{1,*}, Pratikshya Jena^{1,†}, Anish Kumar^{1,‡} and Shradha Mishra^{1§}
¹*Department of Physics, Indian Institute of Technology (BHU), Varanasi, India 221005*
(Dated: February 10, 2026)

Homing and navigation are fundamental behaviors in biological systems that enable agents to reliably reach a target under uncertainty. We present a Reinforcement Learning (RL) framework to model adaptive homing in continuous two-dimensional domain. In this framework, the agent's state is given by its angular deviation from home, actions correspond to alignment or stochastic reorientation, and learning is driven by a radial-distance-based cost that penalizes motion away from the target. For a single self-propelled agent moving with constant speed, we find that the mean homing time $\langle T_{\text{home}} \rangle$ exhibits a non-monotonic dependence on the rotational diffusion strength D_r , with an optimal noise level D_r^* , revealing a subtle interplay between exploration and goal-directed correction. Extending to two agents with soft repulsion, one agent consistently reaches home faster than the other, while in multi-agents system, repulsion ensures separation and the fastest agent becomes progressively faster as group size increases. Finally comparing the mean homing time $\langle T_{\text{home}} \rangle$ of an Active Brownian Particle (ABP) and RL agent over an identical range of D_r , we find that RL trajectories are shorter, less noisy, and consistently faster. Our results show that cost-driven learning, stochastic reorientation, and inter-agent interactions enable efficient adaptive navigation, linking individual and collective homing. This reinforcement learning framework captures key biological features such as feedback-based route learning, randomness to escape unfavorable orientations, and mutual coordination.

I. INTRODUCTION

Homing - the ability of organisms to reliably return to specific locations such as nests, burrows, or dens, is a canonical example of goal-directed spatial navigation in complex and uncertain environments. Across species, this behavior is realized through diverse mechanisms, including path integration in desert ants [1], the combined use of geomagnetic cues and visual landmarks in pigeons [2], and echolocation-based navigation in bats [3], underscoring its evolutionary importance for efficient foraging, reproduction, and survival. In recent years, the study of homing has extended beyond biology, attracting growing interest from robotics, physics, and control theory. Motivated by the work of Paramanick *et al.* [4], which demonstrated that foraging robots exhibit universal statistical features in their homing trajectories largely independent of specific design details, we explore the fundamental principles governing adaptive navigation. Additionally, homing has been studied using computational and theoretical models [5–7], as well as stochastic resetting strategies [8–13] that enhance the search efficiency.

Despite these advances, existing approaches are often limited in their ability to capture adaptive decision-making in uncertain environments: theoretical models rely on predefined navigation rules [14, 15], experiments are limited by biological variability [16], and simulations typically assume fixed stochastic dynamics [17], lacking the flexibility to include learning-driven adaptation.

Reinforcement Learning (RL) provides a natural framework to overcome these limitations by casting homing as a sequential decision-making problem [18, 19]. Unlike supervised learning, which relies on labeled data, or unsupervised learning, which identifies hidden patterns within datasets, RL involves an agent that learns by performing actions, observing their outcomes, and receiving feedback from the environment in the form of cost/reward [20, 21]. And this form works for single as well as multi-agent systems [22–28] where cooperation and competition emerge, making it a powerful framework to study collective homing.

In the present work, we utilized the RL method for active or self-propelling agents/particles. These self-driven particles consume energy to produce directed motion and inherently they are far from equilibrium [29–35]. Within this context, we develop a Q-learning-based RL model that enables a self-propelled agent moving with constant speed to efficiently reach its home location. Among other RL methods—such as SARSA (State-Action-Reward-State-Action) [36, 37], Proximal Policy Optimization [38, 39], and actor-critic algorithms [40, 41]—Q-learning [42, 43] provides a natural and convenient framework for the homing task, as alternative methods often involve on-policy updates or optimized parameterized policies that add unnecessary complexity, whereas Q-learning is simple, fully model-free, and directly updates action values.

We therefore begin by first analyzing the navigation behavior of a single active agent. A central quantity in our analysis is the homing time, T_{home} , which reflects how efficiently an agent returns to its home. In real organisms, T_{home} varies with age, climatic conditions, and physiological state which regulate the stochasticity of motion. In our model, this variability is captured by the rotational diffusion strength D_r , which controls angu-

* riyasingh.rs.phy24@itbhu.ac.in

† pratikshyajena.rs.phy20@itbhu.ac.in

‡ anishkumar.rs.phy22@itbhu.ac.in

§ smishra.phy@iitbhu.ac.in

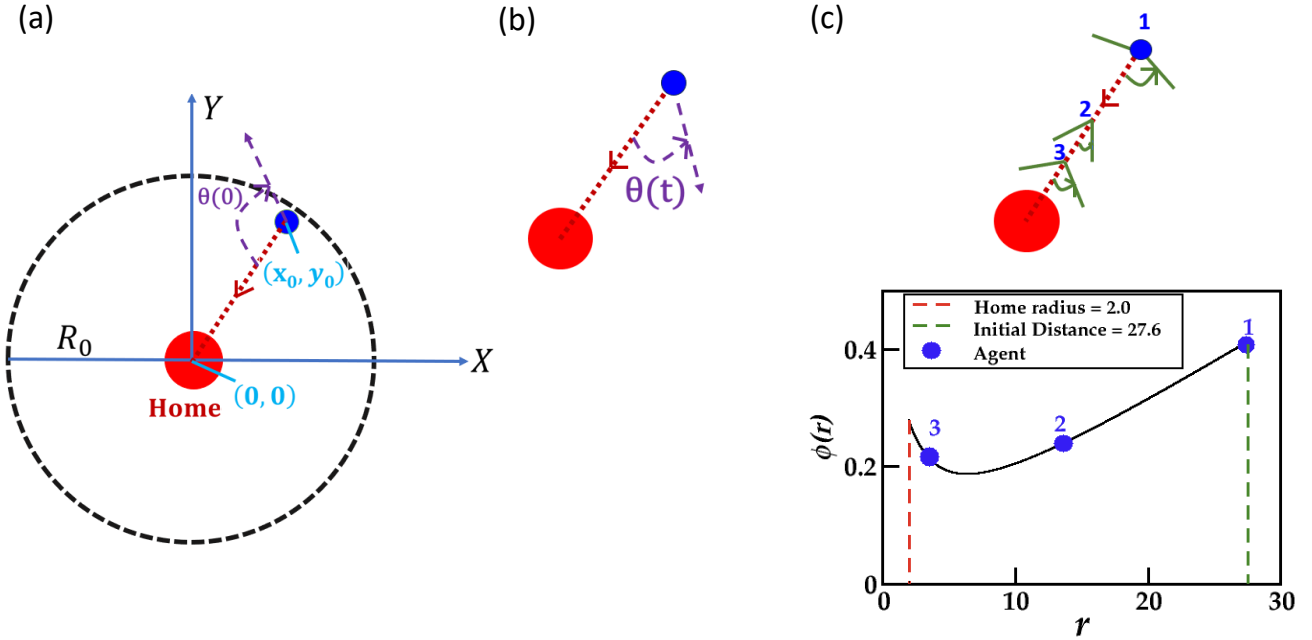


FIG. 1: (a) (Color online) Schematic representation of the homing model showing the circular domain of radius R_0 . The agent (indicated by filled blue circle) starts from an initial position at (x_0, y_0) in the xy -plane, with its initial orientation $\theta(0)$ (shown by purple arrowed dashed line) measured from homing direction taken as reference axis (shown by red arrowed dotted line) from agent towards home (marked by red filled circle at center of domain). (b) Shows the agent's instantaneous orientation as measured from home direction as denoted by $\theta(t)$. (c) The angular threshold ϕ is shown at three representative positions — (1) the initial point, (2) midway along the trajectory, and (3) near the home region corresponding to same three positions marked on plot. The solid green line represents the evolution of the threshold angle ϕ about the home direction, which starts at a large value, decreases to a minimum as the agent aligns towards home, and slightly increases again upon approaching the home location as can be seen in plot also which shows the variation of $\phi(r)$ with distance from the home location. The function is evaluated starting from the initial position (19, 20), corresponding to an initial distance, $r_0 = 27.6$ from home, and continues up to the home region at $r = 2.0$. Thus, the angular threshold gradually decreases as the agent approaches the home position, enforcing greater directional precision in the vicinity of the home while maintaining sufficient freedom for exploration near home.

lar noise and resetting frequency, allowing us to mimic a broad spectrum of biological and physical influences on homing efficiency.

For comparison, we also analyze the corresponding dynamics of an Active Brownian Particle (ABP) subjected to the same angular noise. Across a wide range of D_r , the RL agent consistently achieves shorter homing times and less noisy trajectories than the ABP. Accompanied by distinct dynamical signatures, the resetting statistics show a monotonic increase in both the mean number of resetting events and the effective resetting rate with respect to D_r .

Building on the single-agent dynamics, we extend the model to two-agent and multi-agent systems, where trajectories are coupled through short-range repulsive interactions that prevent overlap and mimic avoidance behavior. We identify three distinct regimes: in the single-agent case, the mean homing time $\langle T_{\text{home}} \rangle$ exhibits a non-monotonic dependence on the rotational diffusion strength D_r , indicating the presence of an optimal noise

level D_r^* ; for two interacting agents, asymmetry emerges, with one agent consistently reaching home faster; and in multi-agent populations, repulsive interactions maintain separation while the fastest agent increasingly outperforms the others as the group size grows.

Together, these regimes reveal general principles of learned navigation that extend from a single agent to interacting groups, offering guidance for both biological studies and the design of engineered active systems. The emergence of faster homing agents in larger groups suggests strategies to improve transport efficiency [44], reduce search times [45], and improve coordinated delivery in both robotic [46] and biomedical applications [47].

The remainder of this paper is organized as follows. In section II, we describe the details of the model, the Q-learning framework, and the state-action definitions. Section III presents the results: single-agent dynamics is analyzed in section III A, followed by two-agents and multi agents extensions in section III B and section III C, respectively. A direct comparison between active

Brownian particle (ABP) and reinforcement-learning (RL) agent is presented in section III D. Finally, the conclusions are summarized in section IV.

II. MODEL

In our model, homing occurs in a continuous two-dimensional circular domain, reflecting the inherently continuous nature of animal and robotic navigation and avoiding lattice artifacts [48, 49]. The spatial extent of the arena is defined as shown in Fig. 1(a) by an effective circular domain of radius R_0 (indicated by the black dashed circle) centered at the origin $(0, 0)$ with reflecting boundary conditions [50]. The agent (shown by a filled blue circle) starts at an initial position (x_0, y_0) inside the domain, away from both the boundary and the home. The home (marked by a filled red circle) is defined as a circular target region of radius $r_{\text{home}} = 2$ centered at the origin.

Consistent with this setup, at each simulation step $t \rightarrow t + \Delta t$, the agent computes its instantaneous radial distance from the home location as:

$$r(t) = \sqrt{x^2(t) + y^2(t)}. \quad (1)$$

where, $\mathbf{r}(t) = (x(t), y(t))$ denotes the position of agent at time t . This radial distance determines the proximity of the agent to the home and serves as the principal spatial variable governing both the cost evaluation and the angular threshold as discussed below.

The agent's orientation is characterized by an angular deviation $\theta(t)$, defined as the minimal signed angle between the agent's heading direction (shown by the purple arrowed dashed line) and the instantaneous direction toward the home (indicated by red arrowed dotted line), which is taken as the reference axis as illustrated in Fig. 1(b). By construction, $\theta(t) = 0$ corresponds to perfect alignment toward the home, while positive (negative) values indicate clockwise (counterclockwise) deviations. The initial orientation of agent $\theta(0) \in [-\pi, \pi]$ is chosen randomly, reflecting the absence of prior directional information. To maintain consistency in orientation dynamics, this deviation is confined to the full interval $[-\pi, \pi]$ rather than $[-\pi/2, \pi/2]$. This modeling choice allows the agent to execute both minor steering corrections and large-angle reorientation, including near-reversals, which are essential in biological and robotic navigation when an agent loses track of its direction or encounters environmental perturbations [51, 52].

To regulate orientation precision, we introduce an angular threshold, $\phi(r(t))$ (shown by green solid lines about the homing direction) as illustrated in Fig. 1(c), which specifies the maximum allowable deviation in the agent's turning angle, $\theta(t)$. All angles are rescaled by π . At each time step, this threshold constrains the allowed reorientation according to:

$$\phi(r(t)) = \frac{\pi}{2} \left(\frac{r(t)}{R_0} \right) + \tan^{-1} \left(\frac{2.0}{r(t)} \right), \quad (2)$$

where R_0 is the radius of the circular domain. The first term introduces a radial dependence that decreases linearly with distance as the agent moves closer to home, thereby decreasing the directional constraint at larger distance from home and allowing greater exploratory flexibility. The second term, $\tan^{-1}(2.0/r(t))$, plays an opposing role: near the home region, it prevents the angular tolerance from collapsing to zero as shown in plot of Fig. 1(c). This ensures that the agent retains a finite acceptance angle even close to the target, avoiding instabilities that could arise if small orientational errors were excessively penalized.

Based on the computed angular deviation, $\theta(t)$ and angular threshold, $\phi(r(t))$ as in Eq. 2, the agent's state is discretized into two classes, thereby minimizing the complexity of the state space while preserving essential decision information. The state variable $s(t)$ is defined as:

$$s(t) = \begin{cases} 1, & \text{if } |\theta(t)| > \phi(r(t)), \\ 2, & \text{if } |\theta(t)| \leq \phi(r(t)). \end{cases} \quad (3)$$

The use of the absolute deviation ensures that only the magnitude of the misalignment determines the state, since clockwise and counterclockwise deviations are equally detrimental from a homing perspective. Physically, these two states represent distinct behavioral modes: state $s(t) = 1$ represents a misaligned configuration in which the agent's heading exceeds the permitted angular threshold and thus requires corrective reorientation to avoid inefficient wandering, whereas state $s(t) = 2$ denotes an aligned configuration in which the agent remains within the angular threshold and needs only minor adjustments to continue progressing towards home.

Such binary state formulations are commonly employed in active search and foraging models, where orientational resets are observed to accelerate convergence and minimize the mean first-passage time [8, 9, 12].

Given its current state, the agent selects an action $a(t) \in \{1, 2\}$ using an ε -greedy policy:

$$a(t) = \begin{cases} \text{random action,} & \text{with probability } \varepsilon, \\ \arg \min Q[s(t), a(t)], & \text{with probability } 1 - \varepsilon. \end{cases} \quad (4)$$

here, the $\arg \min$ operator returns the action $a(t)$ that yields the minimum Q-value among all available actions in state $s(t)$. The ε -greedy strategy promotes a balance between exploration and exploitation [53]: with probability ε , the agent explores by selecting a random action, while with probability $1 - \varepsilon$, it exploits its learned knowledge by choosing the action that minimizes the expected cost. Once an action is chosen, the agent updates its

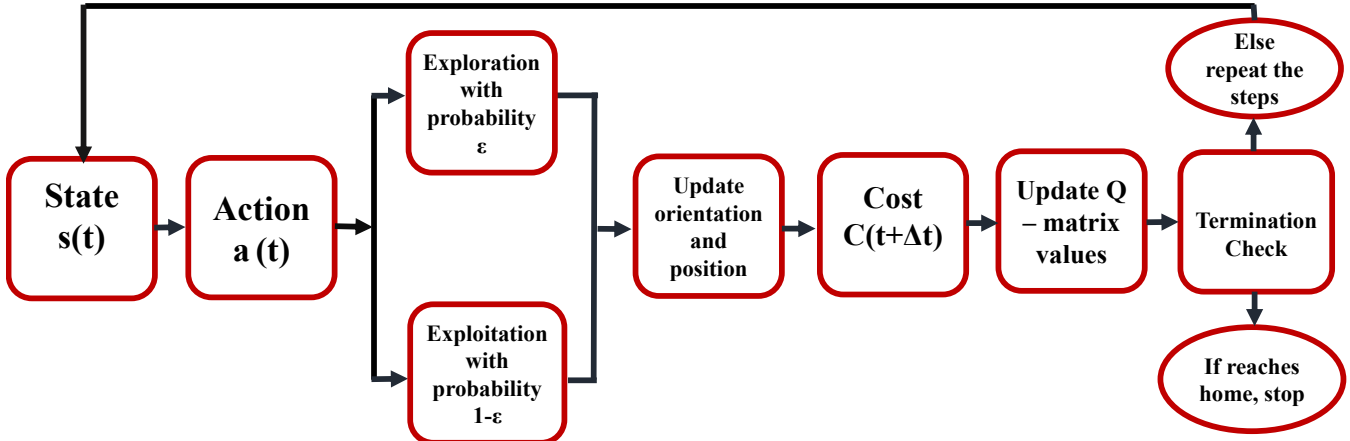


FIG. 2: (Color online) Flowchart illustrating the reinforcement learning (RL) framework used for homing. The algorithm starts from the current state and at each iteration, an action is selected using an ε -greedy exploration-exploitation policy, followed by updates of the agent's orientation and position. The cost is then evaluated based on the distance from the home location, and the Q-values are updated accordingly. A check is performed to determine whether the agent has reached the home; if not, the procedure is repeated from the updated state, otherwise the algorithm terminates.

orientation accordingly:

$$\theta(t + \Delta t) = \begin{cases} 0, & a(t) = 1, \\ \theta(t) + \sqrt{2D_r \Delta t} \zeta, & a(t) = 2. \end{cases} \quad (5)$$

where D_r is the rotational diffusion strength and ζ is a uniformly distributed random variable in the interval $[-\pi/2, \pi/2]$. The bounded range ensures that exploration remains symmetric and moderate, avoiding unrealistic large angle fluctuations within a single update. Both $\theta(t)$ and $\theta(t + \Delta t)$ are defined with respect to the instantaneous home direction, and $\theta(t + \Delta t) = 0$ denotes perfect alignment towards home. Physically, the alignment action ($a(t) = 1$) corresponds to a deterministic corrective turn, steering the agent directly towards home location while the exploratory action ($a(t) = 2$) represents stochastic angular fluctuations.

After updating orientation, the agent's position is advanced using a kinematic rule:

$$\mathbf{r}(t + \Delta t) = \mathbf{r}(t) + v_0 \Delta t \hat{\mathbf{n}}(t + \Delta t), \quad (6)$$

where $\mathbf{r}(t) = (x(t), y(t))$ and $\hat{\mathbf{n}}(t + \Delta t) = (\cos \theta(t + \Delta t), \sin \theta(t + \Delta t))$ is the unit vector in the direction of motion, v_0 is the agent's constant speed and Δt is the discrete time step.

To evaluate the effectiveness of each action within this evolution, we define the cost function, $C(t + \Delta t)$ guiding the learning process based on the change in radial distance resulting from the chosen action. The instantan-

eous cost at time $t + \Delta t$ is defined as:

$$C(t + \Delta t) = |\mathbf{r}(t + \Delta t)| - |\mathbf{r}(t)|, \quad (7)$$

where the cost $C(t + \Delta t)$ is the radial displacement of the agent. This definition ensures that any movement towards home yields a negative cost, while motion away from home produces a positive cost. Because the cost depends only on the change in radial distance, and not on the specific state or action taken, minimizing the cost through Q-value updates thus naturally promotes convergence toward the home location. Since the model consists of two discrete states and two possible actions. Accordingly, the agent is associated with a 2×2 Q-matrix, whose elements—referred to as Q-values—quantify the expected cost of taking a given action in a given state.

The Q-matrix is updated at every time step. Initially, all Q-values are set to zero, and the Q-value associated with the current state-action pair $[s(t), a(t)]$ is updated after each step according to the following equation:

$$Q[s(t), a(t)] \leftarrow (1 - \alpha) Q[s(t), a(t)] + \alpha [C(t + \Delta t)], \quad (8)$$

where α is the learning rate that controls the rate of adaptation. The symbol ' \leftarrow ' denotes an update operation, indicating that the quantity on the left-hand side is reassigned the new value computed on the right-hand side. For ease of comprehension and quick visualization of the methodology, the overall process is summarized in the flowchart as shown in Fig. 2. Over successive iterations, RL mechanism enables the agent to discover an optimal sequence of reorientations that minimize cumulative cost, thereby facilitating reliable homing even in the presence of environmental noise.

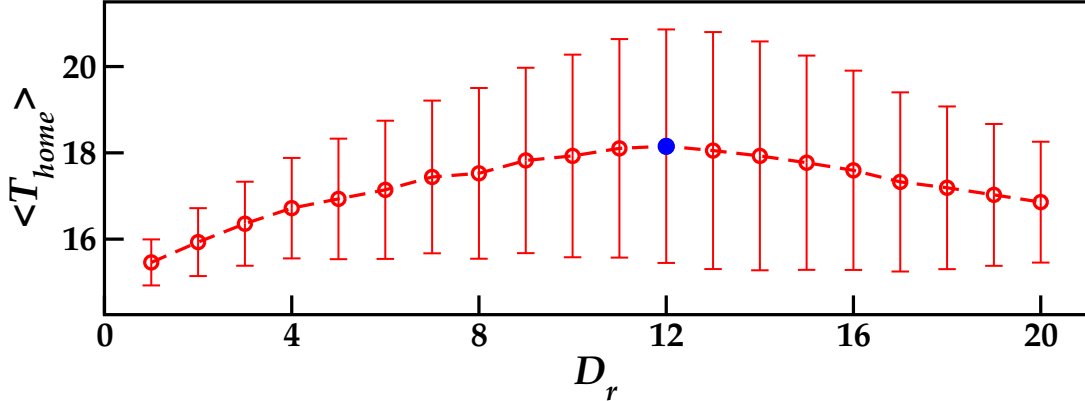


FIG. 3: (Color online) Mean homing time, $\langle T_{\text{home}} \rangle$ vs. rotational diffusion strength, D_r for $\varepsilon = 0.3$ and $\alpha = 0.001$, averaged over 1500 independent realizations. The mean homing time, $\langle T_{\text{home}} \rangle$ initially increases with D_r , then becomes nearly constant over an intermediate range, and finally beyond an optimal value $D_r^* \sim 12$ (blue), the homing time begins to decrease as D_r is further increased. The symbols show the data points and the dashed line is a guide to the eye while error bars indicate the corresponding standard deviations in $\langle T_{\text{home}} \rangle$.

In the simulation, we have used agent's constant speed $v_0 = 0.1$, time step $\Delta t = 0.05$, learning rate $\alpha = 0.001$, and exploration probability $\varepsilon = 0.3$. This choice of α and ε achieves a suitable balance between exploration and convergence stability, consistent with previous RL studies [54, 55]. Extremely large α can cause unstable or divergent Q-value updates, while excessively small values slow convergence and reduce adaptability. Similarly, a moderate ε ensures sufficient stochastic exploration without overwhelming the learned policy. The rotational diffusion strength D_r is varied from 0.5 to 20. The arena has radius $R_0 = 35$, and the agent is initially positioned at distance $r_0 \sim 27$ from the center of the home. This choice avoids trivial cases such as immediate homing from the center or boundary-driven motion due to reflections and provides a meaningful initial condition. A characteristic time scale is defined as the time required for the agent to traverse the domain radius R_0 with its speed v_0 , given by $T_0 = \frac{R_0}{v_0} \Delta t$. All temporal quantities in the analysis are rescaled by this characteristic time scale. For better statistics, unless stated otherwise, all the results are averaged over 1500 independent realizations. Building upon the single-agent Q-learning homing model, we extend the framework to two-agents and multi-agents system by introducing interactions between agents. A full description of the form of interaction potential, initial conditions and size of agents, parameter choices, and implementation details is provided in the Supplementary Material.

III. RESULTS

A. Single-agent Regime

We first focus on the dynamics of a single agent navigating towards home. In our simulation, we explore the effects of the exploration and learning parameter on the

agent's homing performance. Initially, the exploration probability is fixed at $\varepsilon = 0.3$ and the learning rate at $\alpha = 0.001$ to evaluate the agent's homing performance under varying values of D_r . For each D_r value, the mean homing time $\langle T_{\text{home}} \rangle$ is computed.

T_{home} is the time required for the agent to reach a target region of radius $r(t) \leq 2.0$ around the origin, measured in simulation steps and converted to actual time using Δt . The mean $\langle T_{\text{home}} \rangle$ is obtained by averaging over 1500 independent realizations starting from the different initial position and orientation. The initial distance of the agent from the home is chosen in the range $r_0 \sim 27$.

$\langle T_{\text{home}} \rangle$ exhibits a non-monotonic dependence on D_r , it first increases with D_r , then becomes nearly constant over an intermediate range, and finally beyond an optimal value $D_r^* \sim 12$, the homing time begins to decrease as D_r is further increased as shown in Fig. 3. After establishing this baseline, we further investigated the variation of $\langle T_{\text{home}} \rangle$ against D_r for different (ε, α) combinations (see SM Fig. 1 for details).

The error bars associated with $\langle T_{\text{home}} \rangle$ also exhibit a non-monotonic behavior with respect to D_r . For small D_r , the standard deviation is small and increases with D_r , reaching a maximum within an optimal range of D_r , and then decreases again at higher noise levels. At low noise, trajectories are nearly deterministic, yielding similar homing times and small variability. At intermediate D_r , noise competes with learning, producing a wide spread of paths and maximal fluctuations, while at high D_r frequent reorientation leads to statistically similar, diffusive trajectories and reduced variability. To verify that the observed error bars reflect intrinsic properties of the system and are not reducible by averaging over many realizations, we compute the homing time over different independent realizations. (see SM Fig. 2 for details). The error bars remain essentially unchanged, confirming that they are an intrinsic property of the system itself

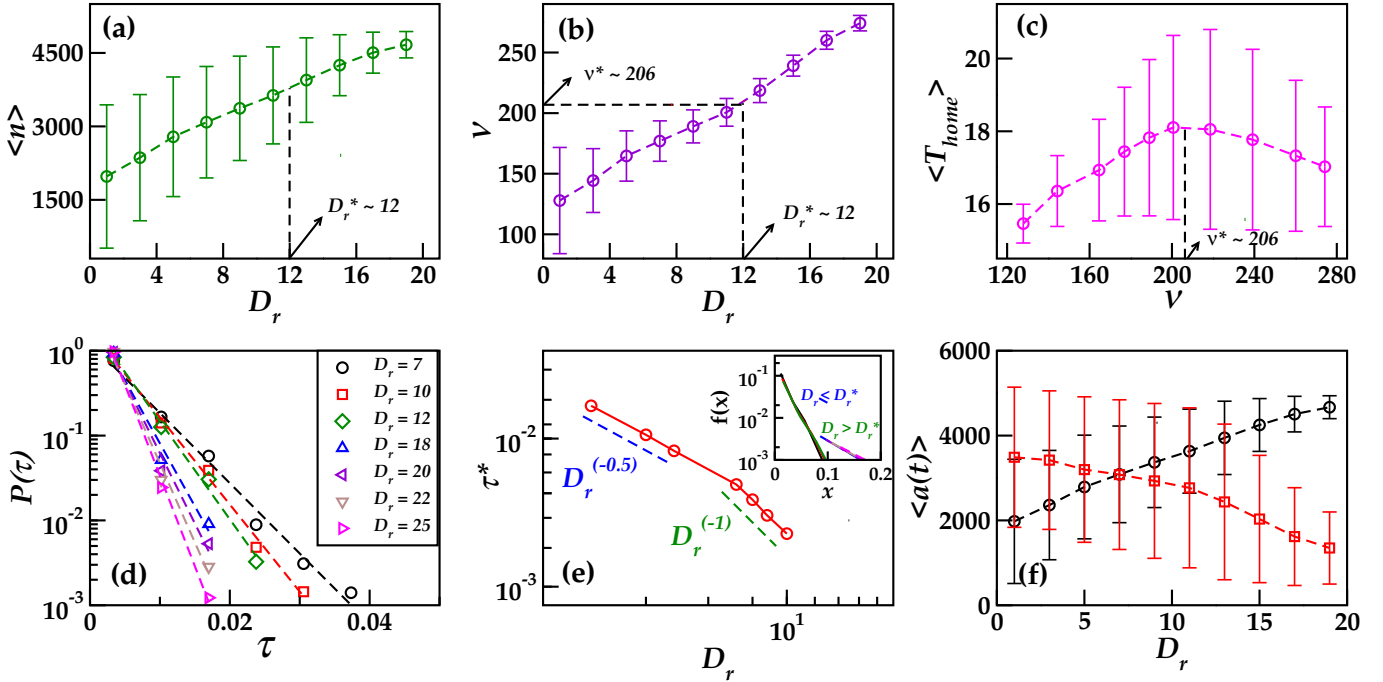


FIG. 4: (a) (Color online) Mean number of resettings $\langle n \rangle$ vs. D_r , averaged over 1500 independent realizations. (b) Frequency of resetting $\nu = \langle n \rangle / \langle T_{\text{home}} \rangle$ vs. D_r (c) Mean homing time $\langle T_{\text{home}} \rangle$ vs reset frequency ν . (d) Probability distribution $P(\tau)$ of time intervals between consecutive resets. (e) The characteristic time τ^* as a function of D_r shows a power-law dependence with two distinct scaling regimes. For $D_r \leq D_r^*$, $\tau^* \sim D_r^{-\alpha}$ with $\alpha = 0.5$, while for $D_r > D_r^*$, $\tau^* \sim D_r^{-\alpha}$ with $\alpha = 1$. The inset shows the collapsed plot of panel (d) using the scaling function $f(x)$ vs. x for $D_r \leq D_r^*$ and $D_r > D_r^*$. (f) Shows the effect of rotational noise D_r on action-selection statistics where black circles and red squares correspond to action 1 and action 2 respectively. Increasing noise drives a crossover in the learned policy, characterized by an enhanced preference for action 1 and a systematic reduction in the selection of action 2. Error bars show the standard deviation in respective quantities in each plot.

rather than a statistical artifact.

We now examine the effect of random resetting on the homing time. In previous studies it is observed that the random resetting can substantially optimize search processes by making the mean first-passage time (MFPT) finite and often minimizing it at an optimal reset rate, thereby improving the efficiency of locating targets compared to search without resetting [56]. To quantify how random resetting affects the homing process, we measure the mean number of resetting events, $\langle n \rangle$ that occur during homing for different values of D_r . In the simulation, a resetting event corresponds to the agent's complete re-orientation towards home direction, implemented when $a(t) = 1$, such that $\theta(t + \Delta t) = 0$ as shown in Eq. 5. This action effectively aligns the agent's heading directly towards the home location.

The results show a steady increase in $\langle n \rangle$ with increasing D_r , continuing even beyond the optimal value $D_r^* \sim 12$ as shown in Fig. 4(a). From this analysis, we define an effective resetting rate, $\nu = \langle n \rangle / \langle T_{\text{home}} \rangle$, which provides a measure of how frequently resettings occur for each D_r . We observe in Fig. 4(b) that ν increases with D_r , indicating that higher rotational noise leads to more frequent reset events. Plotting the mean homing time,

$\langle T_{\text{home}} \rangle$, as a function of ν reveals that it attains a maximum at $\nu^* \sim 206$ as shown in Fig. 4(c). This value of ν^* corresponds to the optimal D_r^* , implying their mutual dependence. We also calculated the probability distribution of time interval between two successive resetting $P(\tau)$, it shows an exponential decay as shown in Fig. 4(d). The characteristic reset time τ^* , obtained from an exponential fit to the probability distribution of time intervals between consecutive resets, is plotted as a function of D_r and found to follow a power-law dependence as shown in Fig. 4(e). We further found that the $P(\tau, D_r)$ shows the two distinct scaling regimes for $D_r > D_r^*$ and $D_r \leq D_r^*$. We found that $P(\tau, D_r) = D_r^\beta f(\tau D_r^\alpha)$, where $f(x) = \exp(-x)$, and from the fitting we found that $(\beta, \alpha) = (1.0, 0.5)$ and $(2.0, 1.0)$ for $D_r \leq D_r^*$ and $> D_r^*$ respectively. The scaled function $f(x)$ is plotted in the inset of Fig. 4(e).

To understand the non-monotonic nature of $\langle T_{\text{home}} \rangle$ and how rotational noise influences decision-making, we examine number of times both the actions as given in Eq. 5 are taken across different D_r , as shown in Fig. 4(f). This behavior demonstrates a clear crossover in action selection, wherein increasing D_r leads to a growing favor for action 1, accompanied by a reduced preference

of selecting action 2. The larger D_r leads to the more deviation from the home direction for action 2 which can bring the system in $s(t) = 1$, unfavorable state for reaching home, as given in Eq.3. That further steer the agent away from the home and agent has to pay a cost for it. The RL agent learn through Q-matrix update as in Eq. 8, and mostly perform the action 1. Hence by increasing D_r further the first action wins over the second one as shown in Fig.4(f).

The observed crossover reflects adaptive noise compensation: as rotational diffusion strength increases, stochastic angular fluctuations render exploratory reorientation unnecessary, favoring deterministic steering that stabilizes homing, analogous to noise-robust navigation strategies in biological organisms that promotes reliance on deterministic cues (e.g., visual landmarks or chemotactic gradients [57, 58]) rather than stochastic search, ensuring reliable homing despite noisy dynamics.

This shift in action selection provides a direct explanation for the observed reduction in the mean homing time $\langle T_{\text{home}} \rangle$ at large D_r as shown in Fig. 3. Since action 1 corresponds to deterministic reorientation towards the home, whereas action 2 introduces stochastic angular updates. The dominance of action 1 at higher D_r therefore suppresses unnecessary stochastic reorientation, leading to more persistent, directed motion and faster convergence to the home region. To further substantiate this mechanism, we analyze the angular dynamics of a representative single realization at different values of D_r . The time series of the angular deviation θ shows that larger fluctuations in θ are associated with an increased selection of action 2, whereas smaller angular deviations predominantly favor action 1. (See SM Fig. 3 for details). Consistently, we find that the standard deviation of the angular deviation, σ_θ , decreases systematically with increasing D_r after optimal D_r^* . (See SM Fig. 4 for details). Despite the increase in the noise strength, the learning dynamics progressively suppress large angular deviations by increasingly favoring action 1, thereby reducing effective orientational fluctuations. This reduction in σ_θ explains the diminished use of stochastic reorientation (action 2) and supports the observed acceleration of the homing process at large D_r .

In summary, the single-agent results reveal that the homing performance depends non-monotonically on D_r . At low noise, trajectories are nearly deterministic with minimal variability, while intermediate D_r leads to the largest fluctuations in $\langle T_{\text{home}} \rangle$ due to strong competition between noise and learning. Beyond a characteristic value D_r^* , frequent reorientations render the motion diffusive but more statistically uniform, causing both the mean homing time and its spread to decrease. The resetting statistics further support this trend: the mean number of resets and the effective reset rate ν increase steadily with D_r , and the reset-interval distribution yields a characteristic time τ^* that follows a power-law dependence giving two different scaling regimes for $D_r \leq D_r^*$ and $D_r > D_r^*$. Now we study the results for the system with

more than one agent.

B. Two-agents Regime

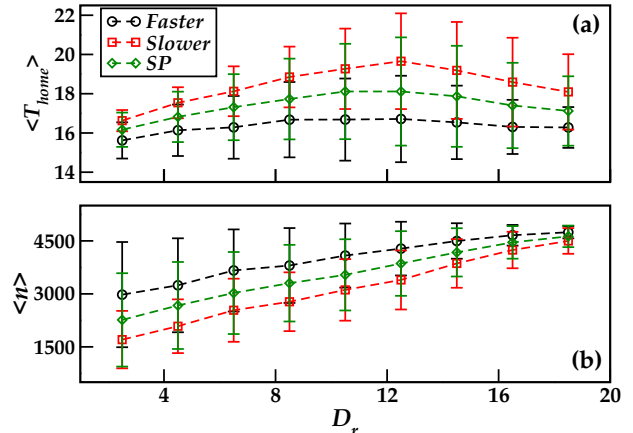


FIG. 5: (a) (Color online) Plot shows $\langle T_{\text{home}} \rangle$ vs. D_r where faster and slower corresponds to faster and slower agents in two-agents system and SP stands for single particle case. (b) Mean number of resetting events $\langle n \rangle$ plotted with respect to D_r where symbols have same meaning as in (a) panel. Error bars show the standard deviation in respective quantities in each plot.

In the two-agents Q-learning system, the homing dynamics exhibit significant variability between the two agents due to their interactions. As shown in Fig. 5(a), in a group of two agents, one particle consistently reaches the home location faster than the other, even outperforming the single-agent case, while the other particle takes the longer time to arrive. Fig. 5(b) illustrates the number of resets for each particle: the faster particle experiences a higher number of resets compared to the single-agent system, whereas the slower particle undergoes fewer resets. Since resets correspond to deterministic reorientations toward the home direction, a higher reset count indicates more frequent corrective alignment, enabling rapid radial progress and thus shorter homing times. In contrast, the slower particle and single agent experience fewer resets, leading to prolonged angular wandering and delayed arrival as shown in Movie 1 (Supplementary Material).

This distinction is further quantified by the standard deviation of the angular deviation, σ_θ , which decreases systematically with increasing D_r beyond the optimal noise strength D_r^* . (See SM Fig. 5(a) for details). Notably, the suppression of orientational fluctuations is most pronounced for the faster particle in the two-agents system, whose σ_θ is significantly smaller than that of both the slower particle and the single-agent case.

In conclusion, the emergence of a faster particle in the two-agent system can be traced to the combined effects

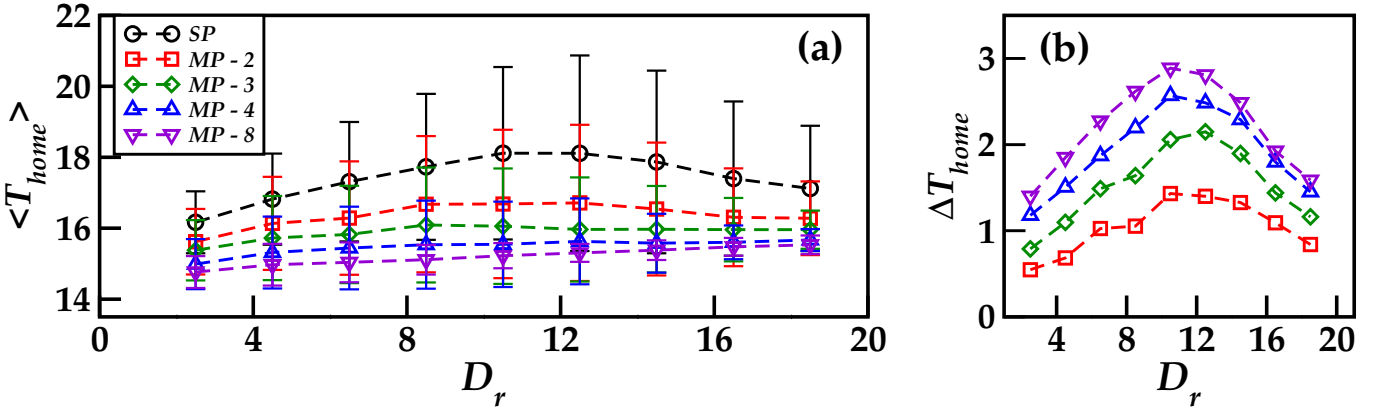


FIG. 6: (Color online) (a) $\langle T_{\text{home}} \rangle$ vs. D_r for different population sizes. SP denotes the single-particle case, while MP- N represents the fastest particle in a group of N agents ($N = 2, 3, 4, 8$). This plot highlights how the fastest particle benefits from increasing group size, showing a systematic decrease in homing time compared to smaller groups and single-particle dynamics. Error bars show the standard deviation in $\langle T_{\text{home}} \rangle$ in each case. (b) For clearer visualization, the difference in $\langle T_{\text{home}} \rangle$ between the fastest agent in MP- N systems ($N = 2, 3, 4, 8$) and the single-particle case (denoted by ΔT_{home}) is shown; symbols correspond to those in panel (a).

of reset statistics and angular stability. The faster particle experiences more frequent resets, leading to deterministic reorientations toward the home direction, which suppress angular fluctuations in $\theta(t)$ and yield a significantly smaller standard deviation σ_θ compared to both the slower particle and the single-agent case. The suppression in orientational fluctuations minimizes angular wandering and sustains persistent radial motion, resulting in faster homing.

C. Multi-agents Regime

For the multi-agents Q-learning system, we observe in Fig. 6(a) that as the number of particles in the group increases, the homing time for the fastest particle decreases. This indicates that the fastest particle becomes increasingly faster in larger groups. For clearer visualization of this effect, the difference in the homing time ΔT_{home} between the single-particle and multi-particle cases is plotted as a function of D_r in Fig. 6(b). This behavior is primarily driven by the increase in the mean number of resetting events with population size as can be seen in Fig. 7.

Notably, the reduction in angular fluctuations in $\theta(t)$ quantified by standard deviation σ_θ , is strongest for the fastest particle when the group size is large (See SM Fig. 5(b) for details). This reduction arises from short-range repulsive interactions between agents. These interactions promote frequent resetting, which suppresses large orientational deviations and repeatedly realigns the fastest agent towards homing direction. In contrast, when the group size is reduced, resetting events become less frequent as can be seen in Fig. 7, and orientational fluctuations become more pronounced, resulting in diminished directional persistence and reduced performance.

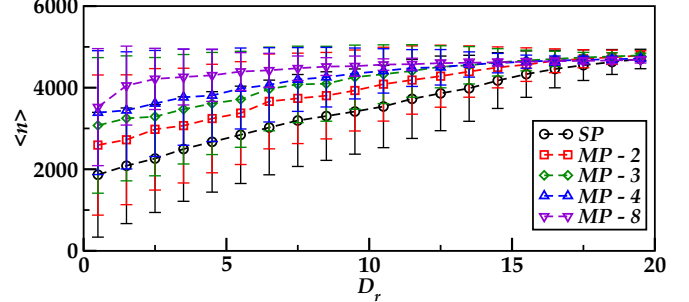


FIG. 7: (Color online) Mean number of resetting events $\langle n \rangle$ plotted with respect to D_r . Error bars show the standard deviation in respective quantities in each plot.

D. RL Vs ABP: Comparison of Homing Efficiency

To provide a baseline for comparing homing performance between Reinforcement Learning (RL)-based agents and purely stochastic dynamics, we introduce an Active Brownian Particle (ABP) model. The goal is to compute the mean homing time $\langle T_{\text{home}} \rangle$ of a non-learning particle so that the RL performance can be quantitatively compared against it. In this model, the particle's movement arises solely from self-propulsion, stochastic angular diffusion, and a predefined state-dependent resetting probability given as :

$$p(t) = \begin{cases} 0, & |\theta| \leq \phi, \\ \frac{|\theta| - \phi}{\pi - \phi}, & \phi < |\theta| < \pi, \\ 1, & |\theta| \geq \pi. \end{cases} \quad (9)$$

At every time step, the particle selects one of the two

possible orientation-update actions based on the above probability $p(t)$.

$$\theta(t + \Delta t) = \begin{cases} 0, & \text{with probability } p(t), \\ \theta(t) + \sqrt{2D_r \Delta t} \eta, & \text{with probability } 1 - p(t). \end{cases} \quad (10)$$

where $\eta(\mathbf{r}, t)$ is a Gaussian white noise with zero mean, $\langle \eta(\mathbf{r}, t) \rangle = 0$, and correlations given by:

$$\langle \eta(\mathbf{r}, t) \eta(\mathbf{r}', t') \rangle = \delta(\mathbf{r} - \mathbf{r}') \delta(t - t'). \quad (11)$$

All other update rules for position and orientation follow the same definitions as in the RL model however, the ABP performs these updates without any learning mechanism—there is no policy optimization, no cost-based adaptation, and no Q-matrix update, and the homing time is computed using the same criterion as in RL. The meanings of all symbols remain identical to those introduced in the RL formulation. By comparing the mean homing time $\langle T_{\text{home}} \rangle$ for ABP and RL across a range of rotational diffusion strengths D_r , the RL trajectories are found to be shorter and less noisy, leading to consistently

$$\langle T_{\text{home}} \rangle_{\text{RL}} < \langle T_{\text{home}} \rangle_{\text{ABP}}.$$

For better visualization of comparison of particle trajectory for RL-agent and ABP, we provide movies of a moving RL-agent and ABP for $D_r = 2, 12$ and 15 . The link for the movie can be accessed through Supplementary Material (Movies: 2, 3 and 4). We clearly see much more wandering of ABP particle in comparison to RL agent.

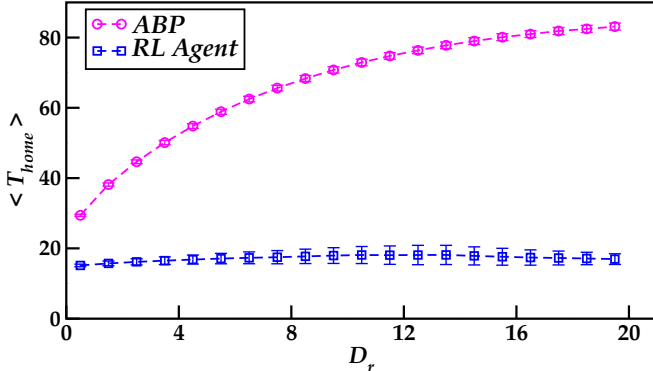


FIG. 8: (Color online) $\langle T_{\text{home}} \rangle$ vs. D_r along with error bars for an ABP and a RL agent. The RL trajectories exhibit consistently shorter homing times than ABP across all noise levels, highlighting the improvement due to learning.

IV. CONCLUSIONS

In this work, we employed a reinforcement learning-based approach to investigate homing dynamics in active

agents, progressing systematically from a single-agent system to interacting two-agent and multi-agent configurations with short-range, spring-like repulsive interactions. The primary objective is to minimize the homing time while accounting for stochastic reorientations. For a single agent, we observe that the mean homing time $\langle T_{\text{home}} \rangle$ exhibits a clear non-monotonic dependence on the rotational diffusion strength D_r , revealing an optimal noise level D_r^* that balances stochastic exploration and learned directional control. At low noise, trajectories are nearly deterministic, whereas intermediate noise leads to enhanced fluctuations due to competition between learning and randomness. Beyond D_r^* , larger reorientations leads to larger cost and results in more frequent resetting and hence reduces both the mean homing time and its variability.

The resetting statistics further support this picture: both the mean number of resetting events and the effective resetting rate increase monotonically with D_r , while the distribution of reset intervals yields a characteristic time scale τ^* that follows a power-law dependence on D_r , with two distinct scaling regimes for $D_r \leq D_r^*$ and $D_r > D_r^*$.

Furthermore, we have compared the homing time obtained from the RL agent with that of a standard Active Brownian Particle (ABP) under identical conditions. The RL-based agent consistently achieves shorter homing times than the ABP, demonstrating its superior efficiency. Extending the model to interacting agents, we find that asymmetry naturally emerges in two-agents system, with one agent consistently achieving faster homing. In larger populations, repulsive interactions maintain spatial separation while collective effects increasingly favor the fastest agent as group size increases. Overall, our results demonstrate that reinforcement learning effectively captures the interplay between stochasticity, resetting, and inter-agent interactions, providing a scalable framework to study efficient homing and navigation in both solitary and collective systems.

In the present work, we have defined the agent's state as the difference between the homing direction and its instantaneous orientation, which provides a simple yet effective representation of the agent's alignment with the target. Alternative formulations, such as polar states (r, θ) as well as velocity-based states can provide a more dynamic sense of progress. However, both these approaches increase the dimensionality of the state space and slow down convergence. Hence, our chosen state definition strikes a practical balance between information content and computational efficiency, allowing the agent to learn effective homing strategies with minimal complexity.

In future extensions of this work, the framework can be advanced by introducing a leader-follower learning mechanism. Such an approach would enable the emergence of collective intelligence and coordinated navigation, allowing slower agents to improve their performance by leveraging information extracted from the most efficient

ACKNOWLEDGMENT

R S, P J, A K and S M thank PARAM Shivay for the computational facility under the National Supercomputing Mission, Government of India, at the Indian Institute of Technology (BHU) Varanasi and also IIT (BHU) Varanasi computational facility. SM thanks DST-SERB India, ECR/2017/000659, CRG/2021/006945 and

CONFLICT OF INTEREST DECLARATION

The authors declare that there are no conflicts of interest.

DATA AVAILABILITY STATEMENT

All data that support the findings of this study are included within the article (and any supplementary files).

[1] R. Wehner, *Journal of Comparative Physiology A* **189**, 579 (2003).

[2] D. Biro, R. Freeman, J. Meade, S. Roberts, and T. Guilford, *Proceedings of the National Academy of Sciences* **104**, 7471 (2007).

[3] C. A. Diebold, A. Salles, and C. F. Moss, *Sensors* **20**, 2958 (2020).

[4] S. Paramanick, A. Biswas, H. Soni, A. Pal, and N. Kumar, *PRX Life* **2**, 033007 (2024).

[5] O. Bénichou, M. Coppey, M. Moreau, P. Suet, and R. Voituriez, *Physical review letters* **94**, 198101 (2005).

[6] F. Bartumeus, M. G. E. da Luz, G. M. Viswanathan, and J. Catalan, *Ecology* **86**, 3078 (2005).

[7] K. J. Painter and T. Hillen, *Journal of the Royal Society Interface* **12**, 20150647 (2015).

[8] M. R. Evans and S. N. Majumdar, *Physical review letters* **106**, 160601 (2011).

[9] M. R. Evans, S. N. Majumdar, and G. Schehr, *Journal of Physics A: Mathematical and Theoretical* **53**, 193001 (2020).

[10] M. R. Evans, S. N. Majumdar, and K. Mallick, *Journal of Physics A: Mathematical and Theoretical* **46**, 185001 (2013).

[11] C. Christou and A. Schadschneider, *Journal of Physics A: Mathematical and Theoretical* **48**, 285003 (2015).

[12] A. Pal and V. Prasad, *Physical Review E* **99**, 032123 (2019).

[13] X. Durang, S. Lee, L. Lizana, and J.-H. Jeon, *Journal of Physics A: Mathematical and Theoretical* **52**, 224001 (2019).

[14] X. Shen, A. Wystrach, U. Gélin, T. Charles-Dominique, and K. W. Tomlinson, *bioRxiv* , 2024 (2024).

[15] E. A. Codling, M. J. Plank, and S. Benhamou, *Journal of the Royal society interface* **5**, 813 (2008).

[16] D. J. Sumpter, in *Collective animal behavior* (Princeton University Press, 2010).

[17] F. Bartumeus and S. A. Levin, *Proceedings of the National Academy of Sciences* **105**, 19072 (2008).

[18] M. Botvinick, S. Ritter, J. X. Wang, Z. Kurth-Nelson, C. Blundell, and D. Hassabis, *Trends in cognitive sciences* **23**, 408 (2019).

[19] V. Mnih, K. Kavukcuoglu, D. Silver, A. A. Rusu, J. Veness, M. G. Bellemare, A. Graves, M. Riedmiller, A. K. Fidjeland, G. Ostrovski, *et al.*, *nature* **518**, 529 (2015).

[20] R. S. Sutton, A. G. Barto, *et al.*, *Reinforcement learning: An introduction*, Vol. 1 (MIT press Cambridge, 1998).

[21] M. Ghasemi and D. Ebrahimi, arXiv preprint arXiv:2408.07712 (2024).

[22] J. Z. Leibo, V. Zambaldi, M. Lanctot, J. Marecki, and T. Graepel, arXiv preprint arXiv:1702.03037 (2017).

[23] Y. Yang and J. Wang, arXiv preprint arXiv:2011.00583 (2020).

[24] X. Wang, Z. Zhang, and W. Zhang, arXiv preprint arXiv:2203.10603 (2022).

[25] Y. Yang, C. Ma, Z. Ding, S. McAleer, C. Jin, and J. Wang, arXiv preprint arXiv:2011.00583 (2025).

[26] K. Zhang, Z. Yang, and T. Başar, *Handbook of reinforcement learning and control* , 321 (2021).

[27] A. Nowé, P. Vrancx, and Y.-M. De Hauwere, in *Reinforcement learning: State-of-the-art* (Springer, 2012) pp. 441–470.

[28] K. Tuyls and A. Nowé, *The Knowledge Engineering Review* **20**, 63 (2005).

[29] M. C. Marchetti, J.-F. Joanny, S. Ramaswamy, T. B. Liverpool, J. Prost, M. Rao, and R. A. Simha, *Reviews of modern physics* **85**, 1143 (2013).

[30] V. Semwal, A. Kumar, J. P. Singh, and S. Mishra, *The European Physical Journal Special Topics* **233**, 3185 (2024).

[31] P. Jena and S. Mishra, *Scientific Reports* **14**, 30831 (2024).

[32] E. Pinçé, S. K. Velu, A. Callegari, P. Elahi, S. Gigan, G. Volpe, and G. Volpe, *Nature communications* **7**, 10907 (2016).

[33] A. Wolf, A. Walther, and A. H. Müller, *Macromolecules* **44**, 9221 (2011).

[34] I. Buttinoni, J. Bialké, F. Kümmel, H. Löwen, C. Bechinger, and T. Speck, *Physical review letters* **110**, 238301 (2013).

[35] M. Brambilla, E. Ferrante, M. Birattari, and M. Dorigo, *Swarm Intelligence* **7**, 1 (2013).

[36] M. Humayoo, arXiv preprint arXiv:2411.14783 (2024).

[37] P. Mohan, P. Narayan, L. Sharma, T. Jambhale, and S. Koul, *International Journal of Recent Technology and Engineering (IJRTE)*. ISSN , 2277.

[38] J. Schulman, F. Wolski, P. Dhariwal, A. Radford, and O. Klimov, arXiv preprint arXiv:1707.06347 (2017).

[39] Z. Wu, C. Yu, D. Ye, J. Zhang, H. H. Zhuo, *et al.*, *Advances in Neural Information Processing Systems* **34**,

26437 (2021).

- [40] V. Konda and J. Tsitsiklis, *Advances in neural information processing systems* **12** (1999).
- [41] Y. Oren, M. A. Zanger, P. R. Van der Vaart, M. M. Çelikok, M. T. Spaan, and W. Bohmer, arXiv preprint arXiv:2406.01423 (2024).
- [42] Y. Jia and X. Y. Zhou, *Journal of Machine Learning Research* **24**, 1 (2023).
- [43] C. J. Watkins and P. Dayan, *Machine learning* **8**, 279 (1992).
- [44] X. Lai, Z. Yang, J. Xie, and Y. Liu, *Multimodal Transportation* **3**, 100164 (2024).
- [45] G. Muñoz-Gil, H. J. Briegel, and M. Caraglio, arXiv preprint arXiv:2503.11330 (2025).
- [46] P. Kormushev, S. Calinon, and D. G. Caldwell, *Robotics* **2**, 122 (2013).
- [47] V. R. Niazmand, M. A. Raheb, N. Eqra, R. Vatankhah, and A. Farrokhi, *Computers in Biology and Medicine* **181**, 109041 (2024).
- [48] A. Dhar, C. Hynén, J. Löfberg, and D. Axehill, arXiv preprint arXiv:2209.14360 (2022).
- [49] A. Dhar, S. Mishra, S. Roy, and D. Axehill, arXiv preprint arXiv:2508.02350 (2025).
- [50] O. Chepizhko, D. Saintillan, and F. Peruani, *Soft Matter* **17**, 3113 (2021).
- [51] I. D. Couzin, J. Krause, N. R. Franks, and S. A. Levin, *Nature* **433**, 513 (2005).
- [52] A. M. Hein, F. Carrara, D. R. Brumley, R. Stocker, and S. A. Levin, *Proceedings of the National Academy of Sciences* **113**, 9413 (2016).
- [53] G. Reddy, A. Celani, and M. Vergassola, *Journal of Statistical Physics* **163**, 1454 (2016).
- [54] A. Kumar, P. K. Mishra, R. Singh, S. Mishra, and D. Giri, *Physica Scripta* **100**, 056009 (2025).
- [55] R. Pramanik, S. Mishra, and S. Chatterjee, *Physical Review E* **111**, 014106 (2025).
- [56] P. C. Bressloff, *Journal of Physics A: Mathematical and Theoretical* **53**, 355001 (2020).
- [57] C. Bühlmann, K. Cheng, and R. Wehner, *Journal of Experimental Biology* **214**, 2845 (2011).
- [58] A. Alonso and J. B. Kirkegaard, *PNAS nexus* **3**, pgae235 (2024).

Supplementary Material: Homing through Reinforcement Learning

Riya Singh^{1,*}, Pratikshya Jena^{1,†}, Anish Kumar^{1,‡}, Shradha Mishra^{1,§}

¹Department of Physics, Indian Institute of Technology (BHU), Varanasi, India 221005

V. DYNAMICS OF TWO AND MULTI-AGENT SYSTEMS

A. Two-agents regime

For the two-agents system, the particles are initially placed at two nearby locations, slightly away from the boundary and at approximately the same radial distance from the home position. The initial distance of each agent from the home is chosen in the range $r_0 \sim 27$. Each particle is assigned a random initial orientation to ensure stochasticity in the initial conditions. All components of the RL scheme - state definitions, ε -greedy action selection, and cost-based Q-table updates - are identical to those used in the single-agent model. The only modification in the two-agents setup is the introduction of finite particle size and short-range repulsive interactions.

In the numerical implementation, the particle positions are updated according to

$$\mathbf{r}_i(t + \Delta t) = \mathbf{r}_i(t) + v_0 \Delta t \hat{\mathbf{n}}_i(t + \Delta t) + \Delta t \sum_j \mathbf{F}_{ij}, \quad (\text{A1})$$

where $\mathbf{r}_i(t) = (x_i(t), y_i(t))$ is the position of particle i , and the unit orientation vector at the updated time is $\hat{\mathbf{n}}_i(t + \Delta t) = (\cos \theta_i(t + \Delta t), \sin \theta_i(t + \Delta t))$. The values of the self-propulsion speed v_0 and the time step Δt are identical to those used in the single-agent case. The resulting interaction force on particle i is $\mathbf{F}_{ij} = -\nabla U(r_{ij})$ where $U(r_{ij})$ is harmonic potential defined as:

$$U(r_{ij}) = \frac{\kappa}{2} (r_{ij} - \sigma_{ij})^2 \Theta\left(1 - \frac{r_{ij}}{\sigma_{ij}}\right), \quad (\text{A2})$$

where $\Theta(x) = 1$ for $x \geq 0$ and 0 otherwise, $r_{ij} = |\mathbf{r}_i - \mathbf{r}_j|$ is the inter-particle separation, and κ is the force constant having value 70. Each particle is assigned a radius $R_i = 0.35$, and repulsion acts only when two particles approach closer than their contact separation $\sigma_{ij} = R_i + R_j$. Repulsive interactions are disabled for any particle that has already reached the home location.

B. Multi-agents regime

For systems with three, four, and eight particles, the initial positions of the agents are chosen such that no particle begins significantly closer to or farther from the home location than the others, while maintaining sufficient spatial separation to avoid immediate overlap. The initial distance of each agent from the home is chosen in the range $r_0 \sim 27$. In all cases, each particle is assigned a random initial orientation to ensure stochasticity in the starting configuration.

All RL components — including the state definitions, ε -greedy action selection, cost-based Q-value updates, the position update rule A1 and treatment of finite-sized particles with short-range repulsive interactions A2 — are identical to those used in the two-agents system. No additional learning parameters are introduced in the multi-agents case.

* riyasingh.rs.phy24@itbhu.ac.in

† pratikshyajena.rs.phy20@itbhu.ac.in

‡ anishkumar.rs.phy22@itbhu.ac.in

§ smishra.phy@iitbhu.ac.in

VI. PARAMETER OPTIMIZATION: EFFECT OF EXPLORATION PROBABILITY (ε) AND LEARNING RATE (α) ON HOMING DYNAMICS

In this section, we analyze the dependence of the mean homing time $\langle T_{\text{home}} \rangle$ on the rotational diffusion strength D_r for different combinations of exploration and learning parameters. Specifically, $\langle T_{\text{home}} \rangle$ is plotted as a function of D_r for three values of exploration probability $\varepsilon = 0.3, 0.4$, and 0.5 , while the learning rate α is varied in the range $\alpha = 0.0005, 0.001, 0.003, 0.005, 0.007$, and 0.01 as shown in SM Fig. 9 (a-c). This systematic exploration allows us to identify the most suitable combination of (ε, α) parameters that produce optimal homing performance for subsequent analysis.

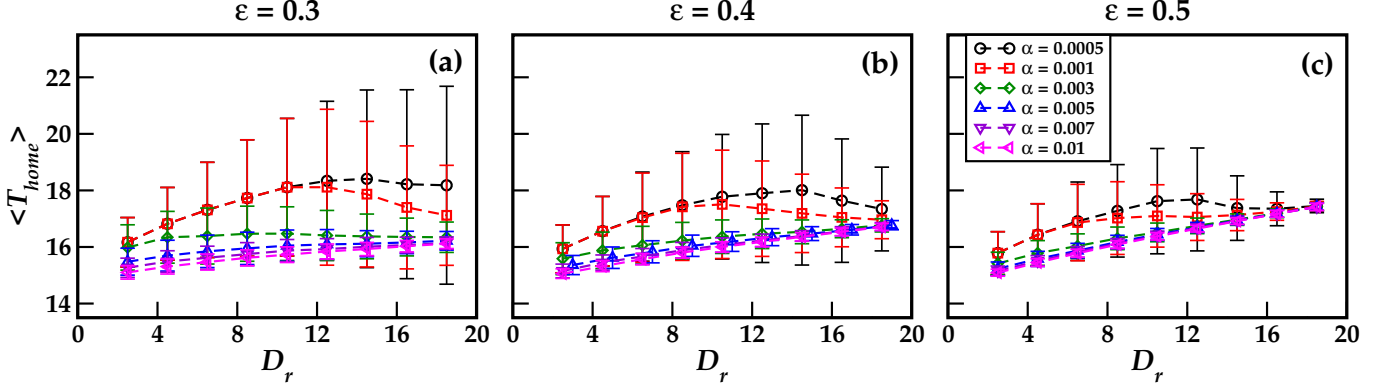


FIG. 9: (Color online) The plots (a-c) show the variation of the mean homing time $\langle T_{\text{home}} \rangle$ against rotational diffusion strength D_r . The three panels correspond to different exploration probabilities $\varepsilon = 0.3, 0.4$, and 0.5 , while each curve within a panel represents a distinct learning rate α ranging from 0.0005 to 0.01 . The symbols show the data points and the dashed line is a guide to the eye while error bars indicate the corresponding standard deviations.

VII. AVERAGING AND ERROR BAR BEHAVIOR

To examine whether the length of the error bars is an intrinsic property of the system or can be reduced by averaging over different realizations, we plot $\langle T_{\text{home}} \rangle$ vs. D_r for $\varepsilon = 0.3$ and $\alpha = 0.001$ across different independent realizations: 50, 500, 1000, and 1500 as shown in Fig. 10 (a-d). The results indicate that increasing realizations does not reduce the error bars; rather the trajectories become more synchronized, suggesting that the variability captured by the error bars reflects inherent system fluctuations.

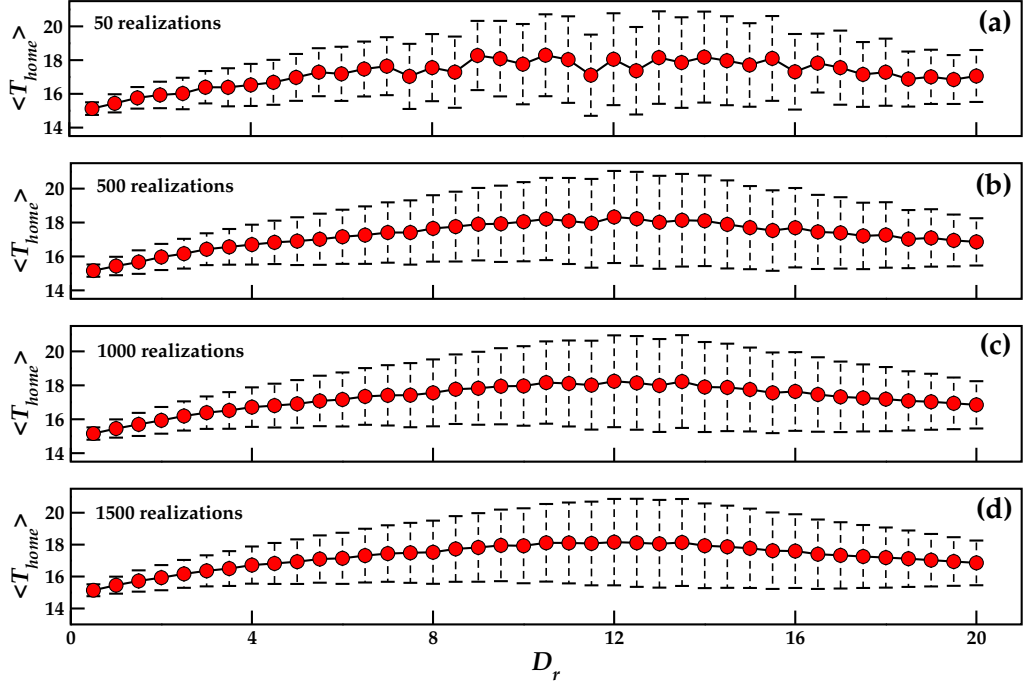


FIG. 10: (Color online) Four panels (a-d) show $\langle T_{\text{home}} \rangle$ vs. D_r for $\varepsilon = 0.3$ and $\alpha = 0.001$ corresponding to different realizations (50, 500, 1000, and 1500). The error bars represent the standard deviation in $\langle T_{\text{home}} \rangle$ for each D_r value within the respective realization.

VIII. EFFECT OF ROTATIONAL NOISE ON ANGULAR DEVIATION AND ACTION SELECTION

In order to examine the effect of rotational noise on angular dynamics and action selection, we analyze the time evolution of the angular deviation $\theta(t)$ and the corresponding action-selection behavior for different values of the rotational diffusion strength D_r . For a single realization, the left panel illustrates the temporal evolution of $\theta(t)$ for D_r values chosen above and below the optimal D_r , while the right panel shows the associated action-selection dynamics, indicating how many times action 1 and action 2 are chosen for the same realization and identical D_r values as in the left panel. Consistent with the observed trends, larger angular fluctuations are correlated with an increased preference for action 2, whereas reduced angular fluctuations are associated with a dominant selection of action 1. This behavior highlights the direct link between suppression in orientational fluctuations and the reinforcement-learning decision-making process.

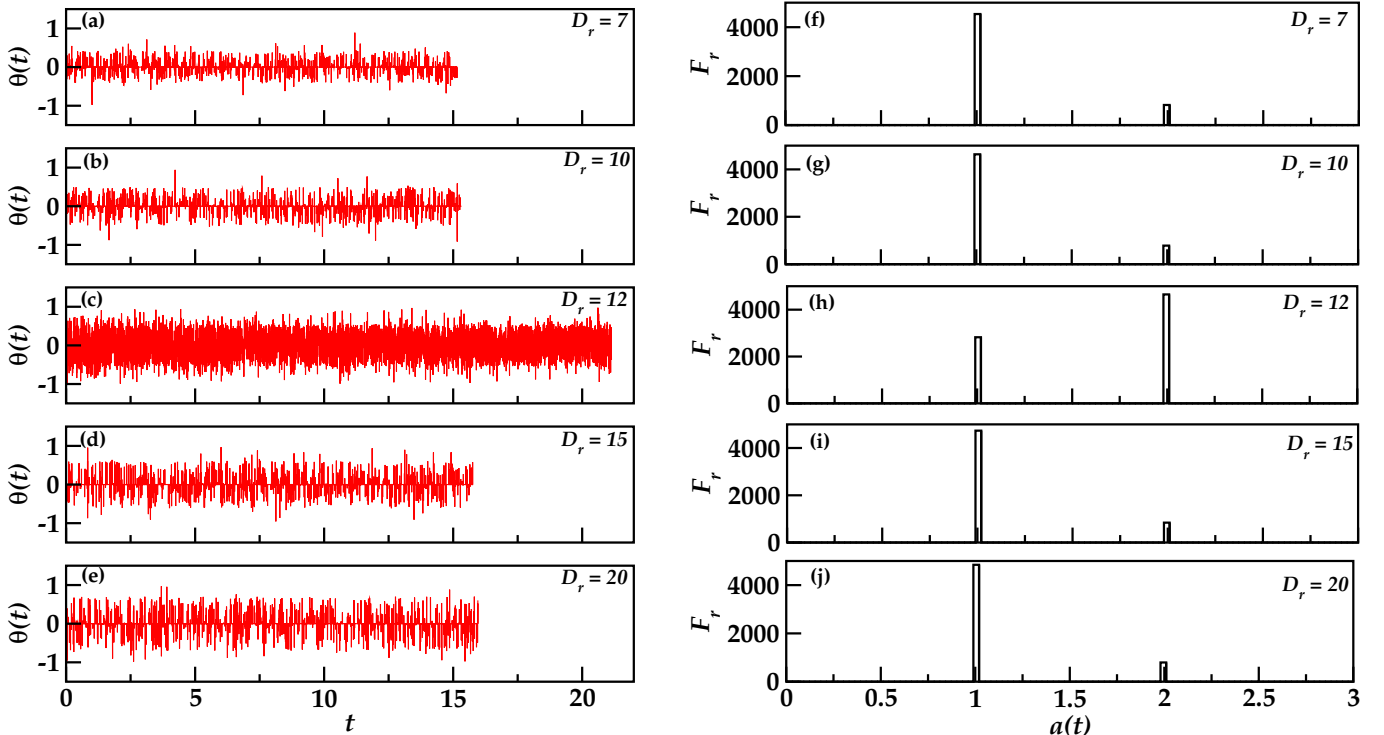


FIG. 11: (Color online) The left panel (a-d) shows the time evolution of the angular deviation $\theta(t)$ from the homing direction for different values of the rotational diffusion strength D_r , chosen above and below the optimal D_r , for a single realization. The right panel (a-d) shows the corresponding action-selection frequency (denoted as F_r) for the same realization and identical D_r values as in the left panel.

IX. STANDARD DEVIATION σ_θ AS A FUNCTION OF D_r : SINGLE AGENT

To understand the decrease in the mean homing time $\langle T_{\text{home}} \rangle$ beyond optimal D_r^* , we analyze the standard deviation of the angular deviation $\theta(t)$ as a function of D_r . The analysis is restricted to regions beyond a radial distance of 2.5 units within a disc of radius $R_0 = 35$, where the home radius is fixed at 2, in order to eliminate the trivial near-home behavior. The calculation is performed over 2000 independent realizations with a time step $\Delta t = 0.05$. The results show that the standard deviation decreases with increasing D_r beyond the optimal value $D_r^* \sim 12$, indicating that frequent resetting lead to a progressively narrower angular distribution $\theta(t)$, corresponding to more localized angular dynamics.

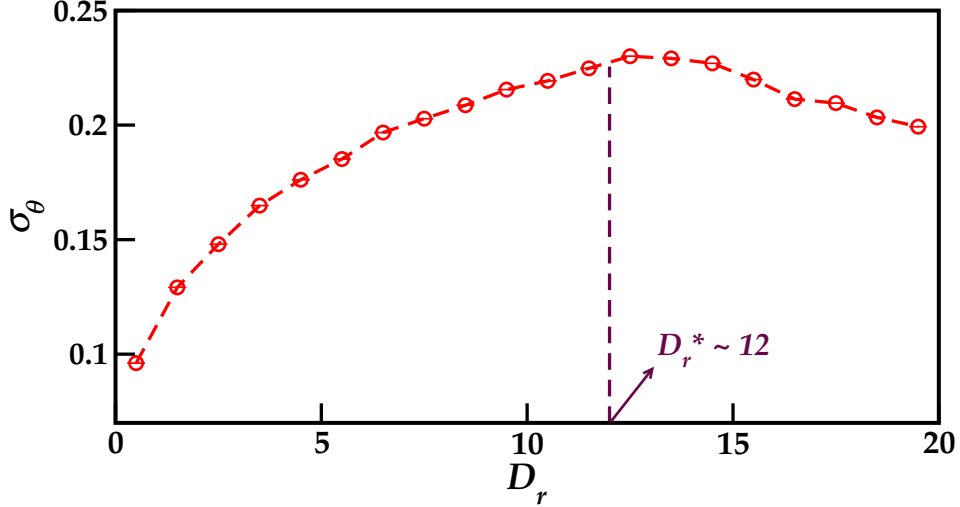


FIG. 12: (Color online) The plot shows the variation of the standard deviation of angular deviation, $\theta(t)$, as a function of D_r for the single-agent system showing narrowing of the angular distribution beyond the optimal D_r^* . Error bars are smaller than the size of the symbols.

X. STANDARD DEVIATION σ_θ AS A FUNCTION OF D_r : MULTI AGENT

To investigate why in a two-agents system one agent exhibits enhanced performance while the other becomes slower—even compared to the single-agent case—we analyze the standard deviation of the angular deviation $\theta(t)$ as a function of D_r , keeping all other simulation parameters identical. The results reveal that although the number of orientation resets increases with D_r , beyond the optimal value D_r^* (of single particle) the distribution becomes progressively narrower, indicating reduced angular fluctuations. This trend suggests that frequent resetting leads to less orientational fluctuations for one particle, while constraining the adaptability of the other. Extending this analysis to a multi-particle system, we observe a consistent behavior: the fastest agent in a larger group exhibits an even smaller standard deviation in $\theta(t)$, confirming that cooperative interactions in larger assemblies further suppresses the orientation fluctuations and enhance the efficiency of the most adaptive agents.

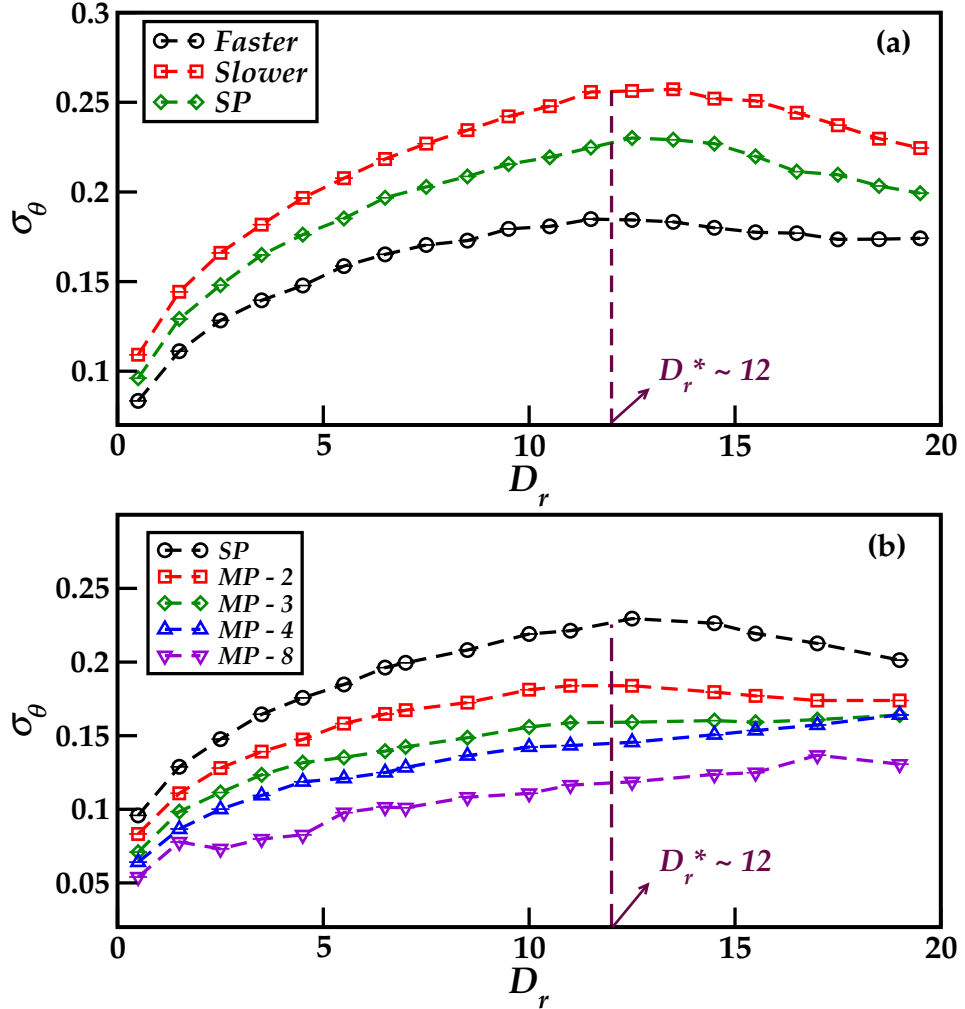


FIG. 13: (Color online) Standard deviation of the angular deviation $\theta(t)$ vs. D_r for (a) the two-agents system and (b) multi-agents system (fastest particle), compared with the single-agent case. Results are averaged over 2000 realizations; error bars are smaller than the symbol size. In (a), SP denotes the single-particle case, while faster and slower indicate the two agents. In (b), MP- N represents the fastest particle in an N -particle system ($N = 2, 3, 4, 8$).

XI. MOVIES OF A TWO-AGENTS SYSTEM AND FOR COMPARISON OF RL AND ABP AT DIFFERENT D_r .

Movie 1: Movie showing the motion of a two-agents system at $D_r = 15$. The RL agents start from nearby locations having the same radial distance from home.

Link:<https://drive.google.com/file/d/1D2iczKqoHdMWGplj3ozjNkV1GXq8c-8D/view?usp=sharing>

Movie 2: Movie showing the motion of a reinforcement-learning (RL) agent and an active Brownian particle (ABP), at $D_r = 2$. The RL agent and the ABP start from different initial positions but at the same radial distance from home.

Link:<https://drive.google.com/file/d/1RdsAi9mYzAo8a6zYD3ezi6W7fvRJyE1X/view?usp=sharing>

Movie 3: Movie showing the motion of a reinforcement-learning (RL) agent and an active Brownian particle (ABP), at $D_r = 12$. The RL agent and the ABP start from different initial positions but at the same radial distance from home.

Link:https://drive.google.com/file/d/1UmTKOLCt_IQNOrZY9akFby1PmAfbNgei/view?usp=sharing

Movie 4: Movie showing the motion of a reinforcement-learning (RL) agent and an active Brownian particle (ABP), at $D_r = 15$. The RL agent and the ABP start from different initial positions but at the same radial distance from home.

Link:<https://drive.google.com/file/d/1CHbjZ1PnL7muZQEprQhpNj2VElpfLC2E/view?usp=sharing>